



Cite this: *Nanoscale*, 2016, **8**, 16995

Size-tunable synthesis of monolayer MoS₂ nanoparticles and their applications in non-volatile memory devices†

Jaeho Jeon,^a Jinhee Lee,^{b,c} Gwangwe Yoo,^d Jin-Hong Park,^d Geun Young Yeom,^e Yun Hee Jang^{*b,c} and Sungjoo Lee^{*a,d}

We report the CVD synthesis of a monolayer of MoS₂ nanoparticles such that the nanoparticle size was controlled over the range 5–100 nm and the chemical potential of sulfur was modified, both by controlling the hydrogen flow rate during the CVD process. As the hydrogen flow rate was increased, the reaction process of sulfur changed from a “sulfiding” process to a “sulfo-reductive” process, resulting in the growth of smaller MoS₂ nanoparticles on the substrates. The size control, crystalline quality, chemical configuration, and distribution uniformity of the CVD-grown monolayer MoS₂ nanoparticles were confirmed. The growth of the MoS₂ nanoparticles at different edge states was studied using density functional theory calculations to clarify the size-tunable mechanism. A non-volatile memory device fabricated using the CVD-grown size-controlled 5 nm monolayer MoS₂ nanoparticles as a floating gate showed a good memory window of 5–8 V and an excellent retention period of a decade.

Received 2nd June 2016,
Accepted 28th August 2016
DOI: 10.1039/c6nr04456e
www.rsc.org/nanoscale

Introduction

Molybdenum disulfide (MoS₂), a two-dimensional (2-d) atomic layered material, has been considered recently for its utility in nanoelectronic applications^{1,2} due to its large band gap energy,^{3,4} high carrier mobility (200 cm² V⁻¹ s⁻¹),¹ and intrinsic n-type conduction properties.^{1,3} MoS₂ has a band gap that can be tuned between 1.9 eV (direct) and 1.2 eV (indirect) by tuning the number of layers present.^{5,6} This attractive band tunability has sparked intense scholarly interest in MoS₂ for its utility in a variety of electronic, optoelectronics, energy storage, and gas sensing applications.^{7–11} Previous studies of

quantum phenomena^{12,13} or 2-d electronic devices^{1,3,14} have been conducted using MoS₂ samples prepared *via* a mechanical exfoliation method^{1,5,14} or chemical vapor deposition (CVD) synthesis.^{15–18} The development of CVD methods for synthesizing MoS₂ has deepened research into 2-d material properties and applications by improving the grain size,¹⁶ control over the layer thickness,^{15,17,18} and scalability.^{15–17} Although 2-d MoS₂ has been widely researched, relatively few studies have examined the synthesis mechanism, material properties, and applications of lower-dimensional MoS₂ (1-d or 0-d). MoS₂ nanoparticles have been considered mainly for their use as electrocatalysts in hydrogen evolution reactions^{19–23} because the MoS₂ edge is a highly activated site for hydrogen evolution, as supported by density functional theory (DFT) calculations.^{24–26} Small MoS₂ nanoparticles have been synthesized using a variety of methods to improve the catalytic effects. Chemical exfoliation has been studied as a promising approach to synthesizing MoS₂ nanoparticles.²⁰ Gopalakrishnan *et al.* reported the size-controlled synthesis of MoS₂ quantum dots by electro-chemical etching bulk MoS₂. However, this approach yielded a narrow range of nanoparticle sizes, 2.5–6 nm.²² CVD synthesis has also been recognized as a practical approach to obtaining MoS₂ nanoparticles. Shi *et al.* developed a size-tunable synthesis of MoS₂ and scalable growth using CVD methods applied to MoO₃ sulfurization.²¹ They reported a range of MoS₂ edge lengths, 0.2–50 μm, on various substrates, such as SiO₂, sapphire, and Au foil. However, this size tunability was limited to the micro-scale

^aSKKU Advanced Institute of Nanotechnology (SAINT), Sungkyunkwan University, Suwon 440-746, Korea. E-mail: leesj@skku.edu

^bDepartment of Energy Systems Engineering, DGIST, Daegu 42988, Korea. E-mail: yhjjang@dgist.ac.kr

^cSchool of Materials Science and Engineering, GIST, Gwangju 61005, Korea

^dSchool of Electronics and Electrical Engineering, Sungkyunkwan University, Suwon 440-746, Korea

^eSchool of Advanced Materials Science and Engineering, Sungkyunkwan University, Suwon 440-746, Korea

† Electronic supplementary information (ESI) available: AFM results (Fig. S1) and Raman spectra (Fig. S2) of CVD grown MoS₂ nanoparticles; hydrogen gas rate dependence of the O 1s XPS spectra (Fig. S3); information of DFT calculation models of different MoS₂ edge states (Fig. S4); I_d–V_g transfer characteristics from the memory device without a floating gate (Fig. S5) and with different MoS₂ nanoparticle floating gates (Fig. S6); floating gate dependence of an average memory window (Fig. S7); and supplementary references. See DOI: 10.1039/c6nr04456e

range. Pavlović *et al.* reported that additional densities of state could be generated within the band gap range *via* the quantum confinement effects in 15 nm MoS₂ nanoparticles.²⁷ The synthesis of MoS₂ nanoparticles smaller than 10 nm has remained a challenge, but these approaches suggested that a wide range of size-tunable and scalable synthesis techniques could be developed to achieve uniformly distributed MoS₂ nanoparticles and to pave the way for device applications with new functionalities. In this work, we report a new size-tunable MoS₂ nanoparticle synthesis method in which CVD was used to vary the size from the nanoscale to the microscale. The MoS₂ nanoparticle size was controlled by varying the ratio of the hydrogen gas in an argon–hydrogen mixture. The controllability, crystalline quality, chemical configuration, and distribution uniformity of the CVD-grown MoS₂ nanoparticles were confirmed using scanning electron microscopy (SEM), atomic force microscopy (AFM), Raman spectroscopy, X-ray photoelectron spectroscopy (XPS), and transmission electron microscopy (TEM) techniques. Non-volatile memory devices were then fabricated using the size-controlled CVD MoS₂ nanoparticles as a floating gate. Performances of size-dependent MoS₂ nanoparticle floating gates were comparatively studied. From 5 nm MoS₂ nanoparticle memory devices, where charge loss in the trapping layer can be suppressed compared to the larger MoS₂ nanoparticle, a memory window of 5–8 V and excellent retention characteristics on the order of a decade

were obtained. Our results demonstrate that size-controlled and uniformly distributed CVD MoS₂ nanoparticles, which are important for future low-dimensional devices and quantum mechanical physics applications, can be obtained by tuning the flow rate of ambient hydrogen.

Results and discussion

We achieve the size-controlled CVD synthesis of MoS₂ nanoparticles on a SiO₂/Si substrate by regulating the ratio of H₂ and Ar in a gas mixture injected into the CVD chamber (the hydrogen gas flow rate was adjusted to vary this ratio). As described in Fig. 1a, the growth of MoS₂ nanoparticles proceeded in a dual temperature zone CVD furnace within a 4 inch quartz tube (see details in Methods). The morphologies of the synthesized MoS₂ nanoparticles were investigated using SEM measurements. Fig. 1b and d show the triangular MoS₂ nanoparticles of size 40–60 nm produced in the absence of hydrogen or at a low partial pressure of hydrogen. The MoS₂ nanoparticle sizes are plotted at several hydrogen flow rates in Fig. 1c, e, g and i. The use of 0 sccm H₂ yielded 70% 50–70 nm MoS₂ nanoparticles (Fig. 1c). Fig. 1e shows that 40 nm MoS₂ nanoparticles were produced under 30 sccm H₂, and 80% of the nanoparticle sizes fell in the range of 30–60 nm. These two results are typical of the sulfurization of vaporized MoO₃ in a

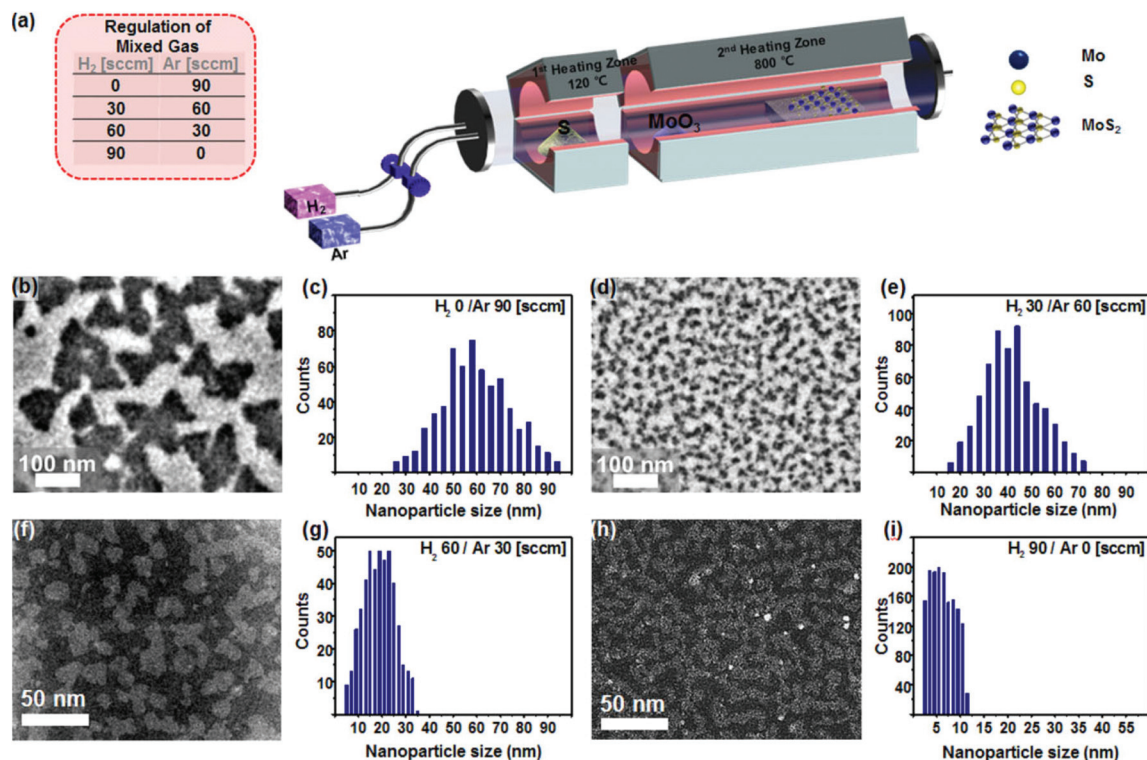


Fig. 1 (a) Schematic diagram of the CVD system used to synthesize the size-controlled MoS₂ nanoparticles under different hydrogen flow rate conditions. SEM images of the CVD-synthesized MoS₂ nanoparticles obtained under (b) 0 sccm, (d) 30 sccm, and STEM images of the CVD-synthesized MoS₂ nanoparticles obtained under (f) 60 sccm, and (h) 90 sccm hydrogen flow rate conditions, and the corresponding histograms of the MoS₂ nanoparticle size distributions (c), (e), (g), and (i), respectively.

CVD chamber during the synthesis of 2-d MoS₂ films.^{15,16,21} By contrast, Fig. 1f and h show arbitrarily shaped MoS₂ nanoparticles, and Fig. 1g and i show an average nanoparticle size of 18 nm and 6.3 nm (81% in the range of 10–30 nm and 90% in the range of 2–10 nm, respectively). It appears that the lateral growth of MoS₂ nanoparticles is blocked at high hydrogen flow rates.

High-resolution transmission electron microscopy (HRTEM) and scanning TEM (STEM) measurements were conducted to determine the edge configurations of the MoS₂ nanoparticles with different sizes. Fig. 2a shows the STEM image of MoS₂ nanoparticles grown in the absence of hydrogen. These particles are 60 nm in size. Although the MoS₂ nanoparticles overlapped during the PMMA transfer process onto the TEM grid, a hexagonal atomic structure was observed (inset of Fig. 2a) in good agreement with previous reports of 2-H MoS₂. Fig. 2b presents the HRTEM image of the atomic structure of the edge configuration of the 60 nm MoS₂ nanoparticle. The hexagonal atomic structure of MoS₂ was elongated to the edge of the nanoparticle. The corresponding selected area electron diffraction (SAED) pattern contains a single set of diffraction spots (inset of Fig. 2b), indicating the presence of single crystalline MoS₂ nanoparticles. The atomic arrangement of the Mo and S centers is apparent because each atom was characterized by a distinct signal intensity in the

high-magnification HRTEM images (Fig. 2b). The intensity profile was used to identify the edge configuration of the MoS₂ nanoparticles. Fig. 2c shows the intensity profile extracted from the red solid line shown in Fig. 2b. The atomic signal intensities of the Mo and S atoms agree well with the atomic arrangement of 2-H MoS₂ (Fig. 2b) and the intensity profile reveals the S₂-terminated edges of the MoS₂ nanoparticles (Fig. 2c). These results agree with the atomic structures expected from the MoS₂ synthesis in the absence of hydrogen gas. On the other hand, the 5 nm scaled MoS₂ nanoparticles grown in the presence of 90 sccm hydrogen display a perfect 2-H hexagonal structure corresponding to the MoS₂ basal plane (Fig. 2d and inset) but a different edge configuration. These nanoparticles were single crystalline, with a single set of diffraction spots measured across the entire nanoparticle (inset of Fig. 2e), but a Mo-terminated edge without S atoms was revealed by the intensity profile spectrum (Fig. 2f) along the red solid line shown in Fig. 2e. This spectrum indicates the absence of sulfur atoms at the edge, probably due to the reduction of sulfur by the high-concentration of hydrogen. The shapes and thicknesses of our CVD-grown size-tunable MoS₂ nanoparticles were characterized using AFM (Fig. S1†) and Raman spectra (Fig. S2†) measurements. It is confirmed that the grown MoS₂ nanoparticles exhibit monolayer characteristics.

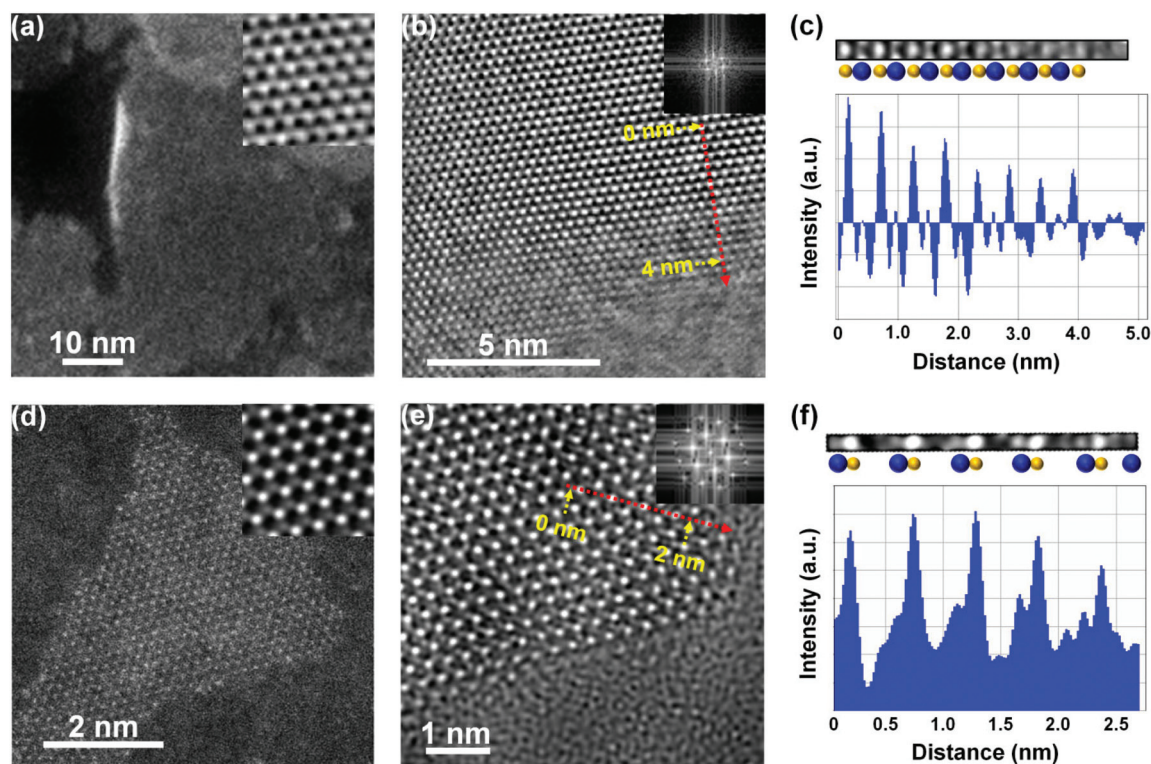


Fig. 2 Scanning TEM images and HRTEM images (insets) of the MoS₂ basal plane as a function of the H₂ flow rate: (a) 0 sccm H₂ (average size: 60 nm) and (d) 90 sccm H₂ (average size: 5 nm). HRTEM images and corresponding FFT electron diffraction patterns (insets) obtained from the edges of the MoS₂ nanoparticles prepared at (b) 0 sccm or (e) 90 sccm H₂. The intensity profile along the lines indicated in images (b) and (e), samples prepared under (c) 0 sccm or (f) 90 sccm H₂.

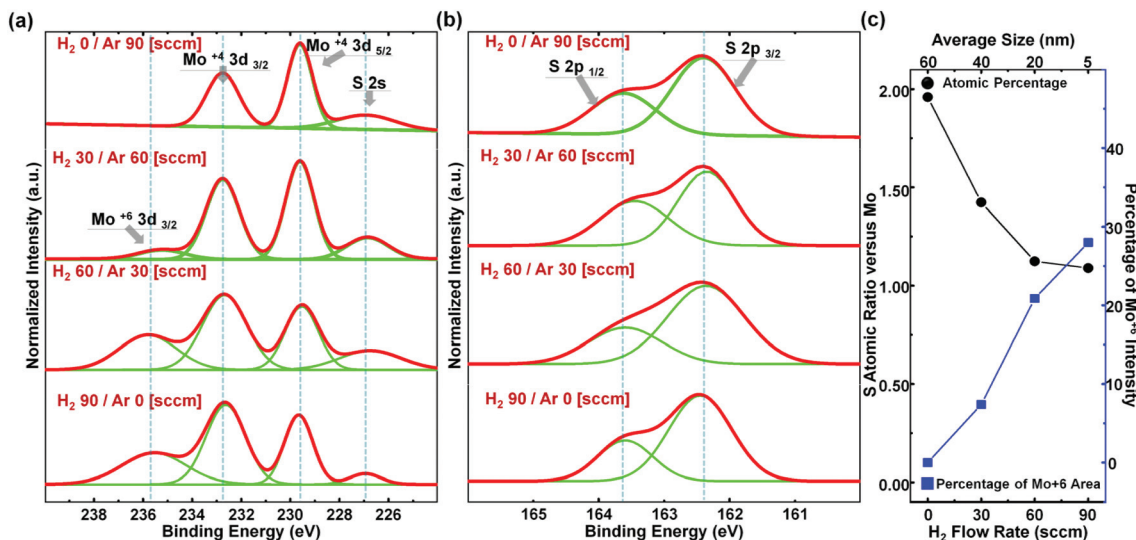


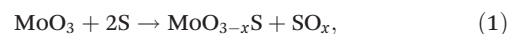
Fig. 3 Angle-resolved (45°) Mo 3d, S 2s (a) and S 2p (b) XPS spectra from MoS₂ nanoparticles and the CVD-synthesized MoS₂ nanoparticles were obtained under different H₂ flow rates: 0 sccm, 30 sccm, 60 sccm, and 90 sccm H₂ respectively, and (c) statistical analysis of the XPS data reveals the S/Mo ratio of the number of atoms and the percentage of the Mo⁶⁺ 3d XPS peak integrated intensity versus the Mo 3d total intensity.

The XPS spectra were measured to investigate the effects of hydrogen on the CVD process. The 45° angle-resolved XPS spectra of Mo 3d and S 2p are shown in Fig. 3. The Mo 3d center in 2H-MoS₂ displays doublet peaks due to 3d_{5/2} at 229.6 eV and 3d_{3/2} at 232.7 eV, corresponding to a Mo⁴⁺ oxidation state, and the peaks at 162.4 eV and 163.6 eV represent 2p_{3/2} and 2p_{1/2}, respectively.^{18,23} Fig. 3a and b reveal peak positions that agree with the above values. The doublets of Mo 3d and S 2p indicate the presence of hexagonally structured MoS₂ crystals under all conditions. A peak at 235.2–235.8 eV was observed in the Mo 3d XPS spectra (Fig. 3a) in the presence of hydrogen. This peak indicates an oxidation state higher than that of Mo⁴⁺, for example, a 3d_{3/2} binding energy corresponding to the Mo⁶⁺ state. This result provides evidence for the formation of a molybdenum oxysulfide structure (MoO_{3-x}S_x) and implies that the hydrogen gas acts as an oxidizer of molybdenum from Mo⁴⁺ to Mo⁶⁺. The binding energy of this peak increases further from 235.2 eV to 235.8 eV under 60 and 90 sccm hydrogen conditions, suggesting an increased number of oxygen atoms bonded to Mo, that is, a greater extent of Mo oxidation, at higher hydrogen flow rates. This is surprising since H₂ has been known as a reducing agent.

The edge state of the synthesized MoS₂ has been extensively studied in the context of hydrogen evolution reaction catalysts.^{23–26} A Mo-terminated edge bearing an attached sulfur dimer (S₂^{δ-}) has been identified as a favorable state in previous studies.^{23,26,28} The attached sulfur dimer (S₂^{δ-}) at the edge has been known to readily react with hydrogen to form H₂S under the action of the Mo catalyst^{23,29} to produce an exposed Mo center without S₂^{δ-}. This effect becomes more pronounced with more abundant hydrogen, enhancing the oxidation of Mo atoms at the edge sites. The partially oxidized Mo edge requires a large amount of energy to elongate the

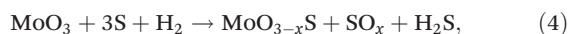
MoS₂ grain size. The above procedure indicates that the MoS₂ nanoparticle size decreases as the hydrogen flow rate increases. Fig. 3c plots the integrated peak intensity ratio of Mo⁶⁺ 3d_{3/2} versus all Mo 3d centers (right axis, blue curve) as well as the atomic ratio of S to Mo (left axis, black curve), as a function of the hydrogen flow rate. Smaller MoS₂ nanoparticles yield higher intensity ratios (0%, 7.4%, 20.8%, or 29.0% under various conditions) due to larger edge fractions. The 0 sccm hydrogen conditions yielded a 1.99 MoS₂ stoichiometry, corresponding to typical MoS₂. The atomic fraction of S decreased with increasing hydrogen due to the reduction of S and the oxidation of Mo. The XPS results reveal the impact of the hydrogen gas on the CVD process. It appears that (1) the hydrogen gas environment produces exposed Mo centers at the nanoparticle edge, (2) these Mo-exposed edges are partially bonded to oxygen to produce Mo⁶⁺ centers, and (3) these oxidized Mo edges grow slowly in the lateral direction to produce small MoS₂ nanoparticles.

In a typical MoS₂ synthesis process, S and MoO₃ powders are vaporized simultaneously by heating in the argon carrier gas. The vaporized MoO₃ is then reduced by vaporized S to form molybdenum oxysulfide species (MoO_{3-x}S).^{29,30} MoS₂ is produced *via* a further sulfurization reaction and nucleation. Finally, the MoS₂ grain grows laterally. This process can be represented by the following reactions:



Previous studies have reported that the edges of the MoS₂ grains in a fully sulfurized condition (eqn (2)) can be viewed as Mo termination fully covered by S dimers (S₂^{δ-}). These attached S dimers as well as the S dimers S₂ (or octamers S₈)

present in the gas phase can be easily reduced by the hydrogen gas with a high chemical potential (μ_{H}). The chemical potential of a species x (μ_x) is proportional to $k_{\text{B}}T \ln P_x$ where P_x is the partial pressure of x , k_{B} is the Boltzmann constant, and T is the temperature, so the presence of hydrogen in the argon carrier gas during the synthesis of MoS_2 can change the chemical reactions by changing the chemical potential. The chemical potential of hydrogen (μ_{H}) would increase as the hydrogen flow rate increases, and under these conditions the hydrogen would act as a reducing agent, and the sulfur, which is either present in the gas phase (as S_2 , S_8 , and so on) or bonded to the MoS_2 nanoparticle edges (as $\text{S}_2^{\delta-}$), would be reduced to form H_2S (eqn (3)), effectively reducing the partial pressure (P_{S}) and in turn the chemical potential (μ_{S}) of sulfur. The chemical potential of sulfur (μ_{S}) is now insufficient for a full sulfurization of MoO_3 , ending up with a deposition of partially reduced (or partially oxidized) MoO_{3-x}S rather than fully reduced MoS_2 , in agreement with the above XPS results indicating a greater amount of molybdenum oxysulfide present on the edge of MoS_2 grown at a higher hydrogen flow rate:



This process can also be viewed as follows. At a higher hydrogen flow rate with a higher chemical potential of hydrogen (μ_{H}), the sulfur dimers ($\text{S}_2^{\delta-}$) at the fully S-covered (or S_2 -terminated) MoS_2 edges (Fig. 4a, case 1) would react more

easily with hydrogen to form H_2S , leaving behind either partially S-covered (or S-bridged) Mo edges (Fig. 4a, case 2) or fully exposed Mo edges, which are then readily oxidized to produce O-covered Mo edges (Fig. 4a, case 3), as previous STM and XPS studies^{23,26,29} have indicated as the stable edge states under varying H_2 flow rate conditions. Once these reactions involving hydrogen have taken place, a significant amount of extra energy would be needed to promote the MoS_2 growth in the lateral direction. The energy requirements for the growth of an additional row of MoS_2 along the different edge states, including the S_2 -terminated edge (case 1, black curve), S-bridged edge (case 2, blue curve), and O-covered edge (case 3, red curve), were calculated using the DFT method (see details in Methods) and presented in Fig. 4a. The growth of an additional MoS_2 row (E_1) was modeled by adding two MoS_2 units to each edge in a unit cell. The binding energy of the two MoS_2 units on each edge to form another row (E_1) was defined as: $E_1 = E[i^{\text{th}} \text{ edge}] + 2E[\text{MoS}_2] - E[(i+1)^{\text{th}} \text{ edge}]$. Geometry optimization after positioning two MoS_2 units on the S_2 -terminated edge (expected under zero or low H_2 flow rates) led to an exothermic and spontaneous growth of a new MoS_2 row ($E_1 = -10.1$ eV, black curve, Fig. 4a), as also suggested in previous studies.^{26,28} In contrast, geometry optimization after positioning two MoS_2 units on the S-bridged and O-covered edges (expected under high H_2 flow rates) did not lead to a spontaneous growth of an additional row, indicating that the bridging S and O adatoms block the adsorption of MoS_2 units to these edges. In fact, the repetitive Mo– S_2 profile and the

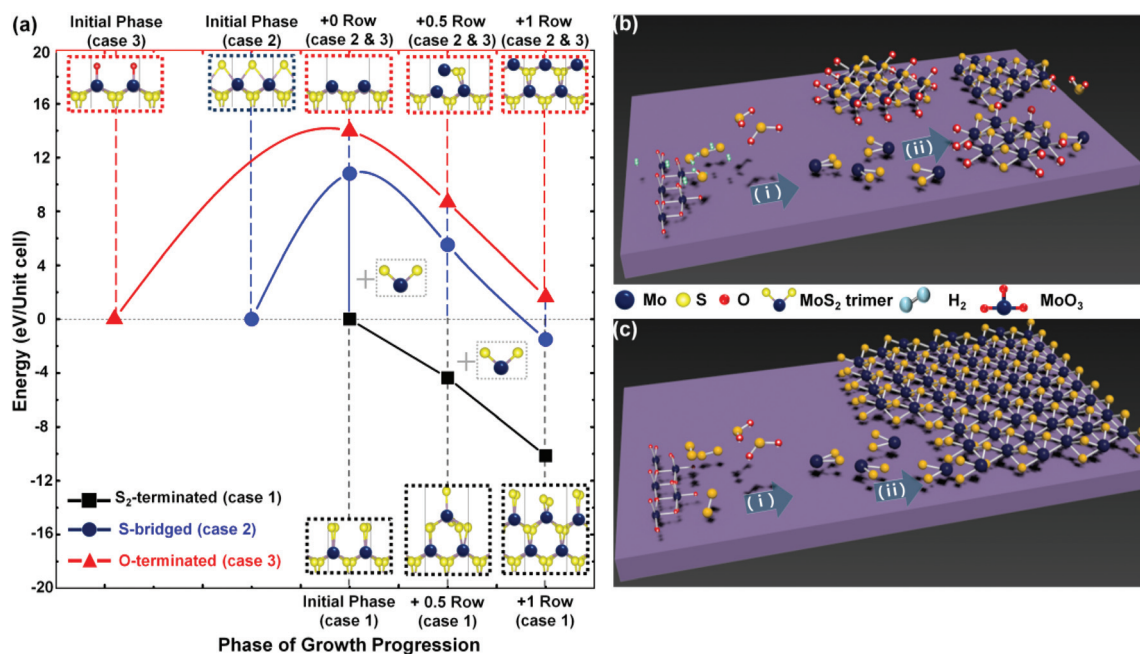


Fig. 4 The growth mechanism of size-controlled MoS_2 nanoparticles. (a) DFT energy profiles for the growth of an additional MoS_2 monolayer row under various synthetic conditions. (Black curve) Exothermic binding of two MoS_2 units to the S_2 -terminated edges abundant under S-rich conditions at low or zero H_2 flow rates. (Blue/red curve) Endothermic detachment of the S/O adatoms from the S-bridged/O-terminated edges, which were abundant under the S-poor conditions at high H_2 flow rates, and the subsequent exothermic binding of two MoS_2 units to the resultant Mo-terminated edges. Schematic illustration of the mechanism during the synthesis of the nano-scale MoS_2 grains under different hydrogen–argon mixtures: (b) without hydrogen or (c) in the presence of abundant hydrogen.

absence of O in the TEM images of the highly crystalline MoS₂ crystals (Fig. 2) also indicate that the bridging S and O adatoms should be first detached to expose Mo-terminated edges for a further growth of the MoS₂ nanoparticles. Indeed, geometry optimization after positioning two MoS₂ units on the Mo-terminated edges led to exothermic and spontaneous growth of an additional MoS₂ row ($E_1 = -12.3$ eV, downhill parts of the blue and red curves, Fig. 4a). However, since the removal of the S and O ad-atoms from these edges to expose the Mo-terminated edges would cost an extra amount of energy ($E_2 = 10.8$ eV from the S-bridged edge and 14.0 eV from the O-terminated edge; uphill parts of the blue and red curves, Fig. 4a) defined as $E_2 = E(\text{Mo-terminated edge}) + 2E(\text{S or O}) - E(\text{S-bridged or O-terminated edge})$, the overall growth of a new row of MoS₂ monolayers on these edges would be either marginally exothermic or endothermic ($E_1 + E_2 = -1.5$ or 1.7 eV; blue and red curves, Fig. 4a). The growth of MoS₂ nanoparticles in the lateral direction at these edge states would be slow and quickly terminated, producing small crystals. The MoS₂ nanoparticles grown at higher hydrogen flow rates are therefore expected to be smaller, in agreement with our observation presented in Fig. 1. The MoS₂ nanoparticle growth is summarized as a schematic diagram in Fig. 4b and c. In the

absence of H₂ (low μ_{H} and high μ_{S}), as shown in Fig. 4b, vaporized MoO₃ units are readily sulfurized by vaporized S to form the S₂-terminated edges (step i) and then the MoS₂ crystals grow quickly in the lateral direction (step ii). Under abundant H₂ conditions (high μ_{H} and low μ_{S}), as described in Fig. 4c, vaporized MoO₃ units are only partially sulfurized to form the S-deficient (S-bridged or O-covered) edges (step i) and then the MoS₂ crystals grow slowly to yield smaller MoS₂ nanoparticles (step ii).

The utility of the MoS₂ nanoparticles as a floating gate in non-volatile memory devices was investigated by fabricating metal/MoS₂/SiO₂/MoS₂ nanoparticle/SiO₂/Si memory structures using MoS₂ nanoparticles of different sizes. Fig. 5a shows a schematic illustration of the fabricated memory device and the inset shows its optical microscopy (OM) image. The $I_{\text{DS}}-V_{\text{CG}}$ transfer curves, where I_{DS} is the source-drain current and V_{CG} is the control gate voltage, were measured to determine the charge trapping capabilities of the MoS₂ nanoparticles and compared to those of a 2-d MoS₂ continuous film. Fig. 5b shows the $I_{\text{DS}}-V_{\text{CG}}$ transfer curves of two floating gates prepared from a monolayer MoS₂ film (triangles) or a 5 nm MoS₂ nanoparticle (stars). The I_{DS} values at the “program” (red symbols) and “erase” (blue symbols) states were measured by

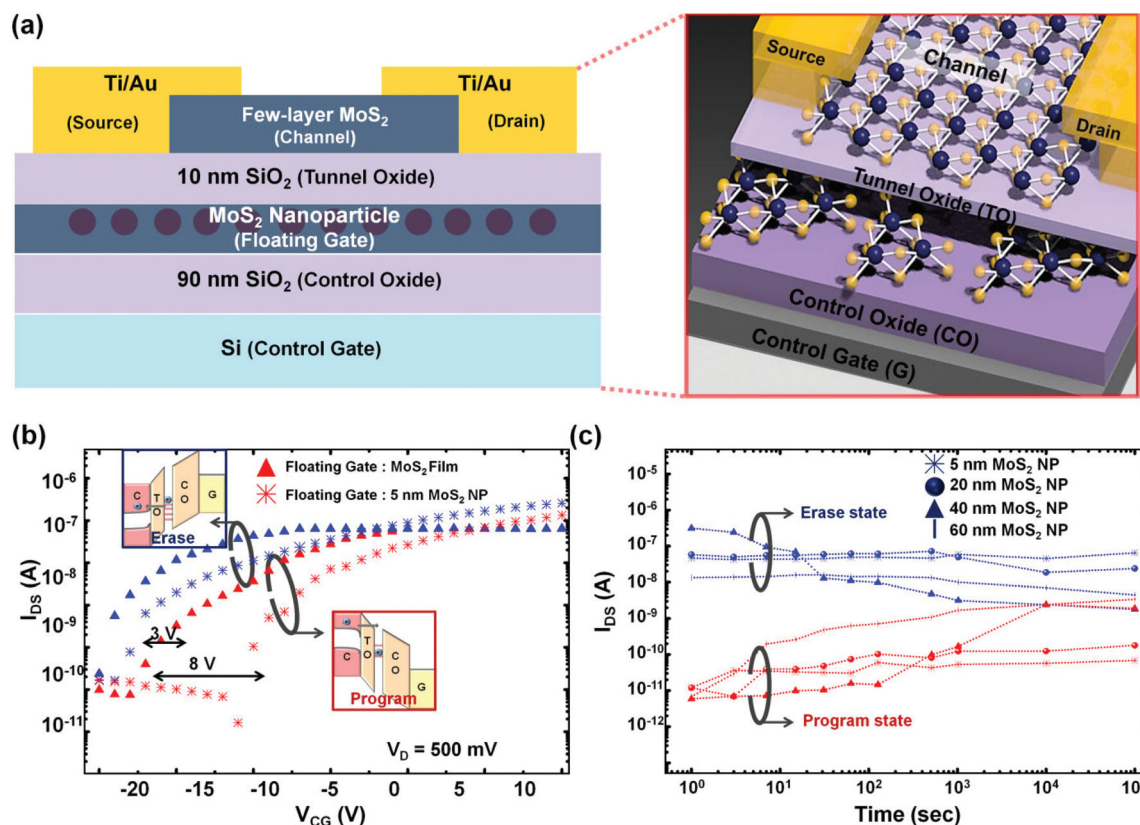


Fig. 5 Transfer and retention characteristics of MoS₂ nanoparticle memory devices. (a) Schematic illustration of the fabricated memory device and OM image (inset). (b) $I_{\text{DS}}-V_{\text{CG}}$ transfer curves obtained at $V_{\text{D}} = 500$ mV under a control gate voltage of +35 V used to “program” (blue symbol) and an applied voltage of -35 V used to “erase” (red symbol); schematic band diagram of the “program” and “erase” states (inset). The squares indicate the transfer curve from the 2-d MoS₂ film floating gate device, the spheres represent the 5 nm MoS₂ nanoparticle floating gate; (c) retention characteristics of MoS₂ nanoparticles of different sizes.

sweeping the V_{CG} over the range -20 to 10 V, after applying a $V_{CG} = +35$ V pulse to program or a $V_{CG} = -35$ V pulse to erase. The threshold voltage (V_{th}) of each device was shifted by around 3 V in the case of the monolayer MoS_2 film floating gate being used and by around 8 V in the case of the 5 nm MoS_2 nanoparticle floating gate, due to the charge trapping effects from the applied program and erase pulses. Memory devices fabricated using MoS_2 nanoparticle floating gates (with nanoparticles of various sizes) displayed several voltage memory windows due to the effects of the floating gate. The V_{th} shift (ΔV_{th}) mainly resulted from the effect of the floating gate because charge transfer of the MoS_2 back-gate FET prepared without a floating gate displayed an absence of ΔV_{th} (Fig. S5†). The application of a positive V_{CG} increased the energy band slope of the tunnel oxide (10 nm SiO_2), and the tunneling barrier thickness decreased. Thus, electrons easily tunneled to the floating gate due to the Fowler–Nordheim tunneling process (inset of the red box in Fig. 5b). The value of V_{th} is shifted by stored charges from the floating gate when in the “program state”. To construct the “erase state”, we applied a negative bias to the control gate, and captured electrons tunneled to the channel (inset of blue box in Fig. 5b). The magnitude of ΔV_{th} was determined by the quantity of charges trapped and could be calculated by $n = (\Delta V_{th} \times C_i)/q$, where ΔV_{th} is the memory window, C_i is the capacitance of the dielectric stack layer, which could be obtained as $C_i = \epsilon_0 \epsilon / d$.³¹ The device prepared with a 5 nm MoS_2 nanoparticle floating gate yielded a trap charge density of $1.9 \times 10^{12} \text{ cm}^{-2}$ ($\Delta V_{th} = 8$ V, $C_i = 3.837 \times 10^{-8} \text{ F cm}^{-2}$). The 5 nm monolayer MoS_2 nanoparticle floating gate provided a larger memory window than is obtained from Si or Ge nanocrystals.^{32–35} The memory window was comparable in size to that obtained from nanoscale graphene floating gates.³⁶ Previous reports have indicated that the charge trapping capabilities of semiconductor nanocrystals decreased as the nanoparticle size decreased^{36,37} due to an increase in the total quantum confinement energy and a decrease in the available density of states, because the particles were smaller in size than the Bohr radius of the semiconductor (Si = 4.9 nm, Ge = 24.3 nm). The monolayer MoS_2 , by contrast, has a very small Bohr radius (0.602 nm);³⁸ thus, the charge trapping capacity is not restricted in MoS_2 nanoparticles a few nm in scale. We calculated an average memory window across more than 10 devices prepared under each of the conditions (Fig. S7†). The size of the memory window increased as the MoS_2 nanoparticle size decreased, suggesting that the available size-dependent charge trap sites were comparable to the estimated edge density of each MoS_2 nanoparticle. Defects from the edges of the MoS_2 nanoparticles acted as the main charge trap regions. Thus, the use of a 2-d MoS_2 film as a floating gate yielded a device with the smallest trapped charge density. A larger trapped charge density could be obtained using a floating gate prepared from smaller MoS_2 nanoparticles. The memory window could, therefore, be controlled by tuning the size of the MoS_2 nanoparticles. Similar results have been observed in previous nanoscale graphene floating gate studies.³⁶ We measured the time-dependent

I_{DS} during the program and erase states over a time duration of 10^5 s, as shown in Fig. 5c. The use of the large MoS_2 nanoparticles as a floating gate yielded a short retention time, probably due to the charge recombination effects^{33,39,40} from the large nanoparticles. Strong charge retention behaviors and an adequate program/erase ratio of 10^4 were obtained from the smaller MoS_2 nanoparticle floating gate, with charge losses of 11.77% and 20.16% after 10 years predicted for the 5 nm and 20 nm MoS_2 nanoparticle floating gates, respectively. These values were not only higher than those of other MoS_2 films and graphene floating gates,^{31,41,42} but were comparable to those of the noble metal quantum dot floating gate materials (Au).⁴³ The strong retention characteristics were attributed to the strong Coulomb blockage energy and a reduction of the interlayer charge recombination due to the nanoparticle size of a few nm.³³

Conclusions

In conclusion, we demonstrated the CVD synthesis of monolayer MoS_2 nanoparticles with lateral sizes controlled over the range 5 – 60 nm. The size control of the nanoparticles was achieved by modifying the hydrogen flow rate in the CVD process. DFT calculations were used to explain the CVD growth mechanism at different H_2 gas contents. The monolayer MoS_2 nanoparticles were uniformly deposited over a SiO_2 substrate on the centimeter scale, and each basal plane of MoS_2 nanoparticles displayed a crystalline structure that agrees with the structure reported for typical MoS_2 films, as confirmed by Raman and XPS, SEM, AFM, and TEM analyses. These MoS_2 nanoparticles performed outstandingly as floating gates in non-volatile memory applications. Non-volatile memory devices fabricated using the 5 nm MoS_2 nanoparticles as a floating gate layer, in particular, exhibited a large memory window of 5 – 8 V and excellent retention characteristics, proving that our method to synthesize MoS_2 nanoparticles is simple but extremely tunable and useful for device fabrication.

Methods

Growth and characterization of the MoS_2 nanoparticles

The growth of MoS_2 flakes was carried out in a dual zone thermal CVD furnace with a 4 inch quartz tube. The sulfur powder (Alfa Aesar 99.999% , 200 mg) was placed in the 1st heating zone, located upstream, within an alumina boat, and the other precursor, the MoO_3 powder (Alfa Aesar 99.995% , 10 mg), was placed in the center of a 2nd heating zone. Prior to conducting the CVD synthesis process, the 90 nm thick SiO_2/Si substrates were cleaned with acetone, IPA, and DI water for 15 minutes. The cleaned substrates $1.5 \text{ cm} \times 1.5 \text{ cm}$ in size were placed 12 cm from the edge of the MoO_3 -containing alumina boat. After purging the chamber with Ar gas for 10 minutes, the 1st heating zone was heated to 120 °C (rate of temperature increase: 1.58 °C min^{-1}) and the 2nd heating

zone was heated to 800 °C (rate of temperature increase: 13 °C min⁻¹) under the H₂-Ar gas mixture. This mixed gas was prepared by varying the H₂ and Ar gas flow rates within a fixed total gas flow rate of 90 sccm (see Fig. 1a). Each MoS₂ nanoparticle batch was synthesized at 800 °C over 20 minutes. We utilized this fixed growth condition because the best controllability of MoS₂ nanoparticle size was obtained under this condition by varying hydrogen flow rates. The hydrogen flow rates (0, 30, 60, and 90 sccm) yielded nanoparticles of size 60, 40, 20, and 5 nm, respectively. After the thermal CVD process, the chamber was cooled to room temperature. During the growth procedure, Ar gas was used to carry the vaporized precursors, and hydrogen gas played a role in triggering the surface chemical reaction. Previously, chemical sulfurization reactions were explained as transforming Mo metal to MoS₂ nanoparticles. The morphologies of the MoS₂ nanoparticles were determined by the chemical potential of S (μ_S), which was controlled by tuning the partial pressure of hydrogen in the synthesis atmosphere. Here, we observed that the MoS₂ particle size was controlled by the H₂ flow rate, suggesting that the chemical reaction between MoO₃ and S was controlled by the H₂ flow rate through modification of the chemical potential of S (μ_S). Thus, MoS₂ growth during the CVD process could be controlled by varying the H₂ flow rate. The surface morphologies of the samples were examined with an atomic force microscope (Veeco Icon) and a scanning electron microscope (JEOL JSM-7401F). Raman spectra were obtained with a confocal Raman microscopic system (Witec Alpha 300 M+). The wavelength and power of the laser were 532 nm and 2 mW respectively. The grating of the spectrometer was set at 1800 g mm⁻¹ for the Raman spectra. The TEM samples were prepared with a transfer process using buffer oxide etcher (BOE) solution to place the 5–100 nm MoS₂ nanoparticles onto an amorphous carbon supported Cu grid. TEM and STEM images were obtained with the HRTEM (JEOL JEM ARM 200F) by using an incident electron beam energy of 80 kV. The chemical configurations were determined by using angle resolved X-ray photoelectron spectroscopy (ESCA2000, VG Microtech Inc.) with an Mg K α X-ray.

DFT calculations

Three different MoS₂ monolayer edge states were represented using periodic slab models. These models were built by redefining the hexagonal lattice of the (0001) basal plane ($a = b = 3.16$ Å) of the MoS₂ crystal to form an orthorhombic lattice ($a = 3.16$ Å, $b = 5.47$ Å), and a vacuum layer of 20 Å in the c direction was inserted to create a two-dimensionally periodic MoS₂ (0001) monolayer without introducing interactions with its periodic image. The (2 × 2) supercell was constructed, and a vacuum layer of 9.12 Å in the b direction was inserted to create a one-dimensionally periodic four-MoS₂-row band with an S₂-terminated top edge and a Mo-terminated bottom edge. Various synthetic conditions and growth stages were modeled by varying the states of the top edge (*e.g.*, removing S or S₂ and adding O or MoS₂ units). The bottom two MoS₂ rows were fixed at the bulk positions (and accordingly, the lattice

parameters were fixed at the bulk values, $6.32 \times 12.3 \times 30.9$, in Å). The atomic positions at each state were fully optimized using the spin-polarized DFT with the Perdew–Burke–Ernzerhof exchange–correlation functional combined with the D3 dispersion correction of Grimme (PBE-D3)^{44–46} implemented in VASP 5.3.5.⁴⁷ The core electrons were replaced by the projector-augmented-wave (PAW) pseudopotentials, and the valence electrons (6 in Mo 5s/4d and 6 in S 3s/3p) were represented by plane-wave basis sets with a kinetic energy of up to 600 eV. The $4 \times 1 \times 1$ Monkhorst–Pack mesh⁴⁸ was used for the k -point sampling. The Brillouin zone was integrated using the Gaussian smearing method with a 0.2 smearing width σ . The energy convergence criterion for ionic relaxation was set to 10⁻⁴ eV.

Device fabrication and characterization

Non-volatile memory devices were fabricated with CVD grown MoS₂ nanoparticles as the floating gate. MoS₂ nanoparticles were synthesized on 90 nm thick SiO₂/Si substrates, which worked as a control gate dielectric and gate electrode. A 10 nm thick SiO₂ layer was deposited using e-beam evaporation methods to form a tunneling oxide. The channel material (few-layer MoS₂) was exfoliated onto the PMMA/PVA substrate and transferred onto the e-beam-deposited SiO₂. After removing the PMMA/PVA, using e-beam lithography, electron-beam evaporation, and a lift-off process, the Cr/Au (5/50 nm) source and drain electrodes were patterned on the MoS₂ channels. The channels of these memory devices are 1 μ m in width and 1 μ m in length. The fabricated memory devices were analyzed through electrical measurements by using a Keithley 4200 semiconductor parameter analyzer.

Acknowledgements

This research was supported by the Global Frontier Program through the Global Frontier Hybrid Interface Materials (2013M3A6B1078873, 2013M3A6B1078882), the Pioneer Research Center Program (2014M3C1A3053024), and the Basic Science Research Program (2015R1D1A1A09057297, 2015M3A7B7045496) through the National Research Foundation of Korea funded by the Ministry of Science, ICT & Future Planning.

References

- 1 B. Radisavljevic, A. Radenovic, J. Brivio, V. Giacometti and A. Kis, *Nat. Nanotechnol.*, 2011, **6**, 147–150.
- 2 Q. H. Wang, K. Kalantar-Zadeh, A. Kis, J. N. Coleman and M. S. Strano, *Nat. Nanotechnol.*, 2012, **7**, 699–712.
- 3 S. Kim, A. Konar, W.-S. Hwang, J. H. Lee, J. Lee, J. Yang, C. Jung, H. Kim, J.-B. Yoo, J.-Y. Choi, Y. W. Jin, S. Y. Lee, D. Jena, W. Choi and K. Kim, *Nat. Commun.*, 2012, **3**, 1011.
- 4 S. Lebegue and O. Eriksson, *Phys. Rev. B: Condens. Matter*, 2009, **79**, 115409.

- 5 W. S. Yun, S. W. Han, S. C. Hong, I. G. Kim and J. D. Lee, *Phys. Rev. B: Condens. Matter*, 2012, **85**, 033305.
- 6 K. F. Mak, C. Lee, J. Hone, J. Shan and T. F. Heinz, *Phys. Rev. Lett.*, 2010, **105**, 136805.
- 7 W. Choi, M. Y. Cho, A. Konar, J. H. Lee, G.-B. Cha, S. C. Hong, S. Kim, J. Kim, D. Jena, J. Joo and S. Kim, *Adv. Mater.*, 2012, **24**, 5832–5836.
- 8 J. Xiao, D. Choi, L. Cosimbescu, P. Koech, J. Liu and J. P. Lemmon, *Chem. Mater.*, 2010, **22**, 4522–4524.
- 9 Q. He, Z. Zeng, Z. Yin, H. Li, S. Wu, X. Huang and H. Zhang, *Small*, 2012, **8**, 2994–2999.
- 10 D. J. Late, Y.-K. Huang, B. Liu, J. Acharya, S. N. Shirodkar, J. Luo, A. Yan, D. Charles, U. V. Waghmare, V. P. Dravid and C. N. R. Rao, *ACS Nano*, 2013, **7**, 4879–4891.
- 11 H. Wang, L. Yu, Y.-H. Lee, Y. Shi, A. Hsu, M. L. Chin, L.-J. Li, M. Dubey, J. Kong and T. Palacios, *Nano Lett.*, 2012, **12**, 4674–4680.
- 12 J. P. Wilcoxon and G. A. Samara, *Phys. Rev. B: Condens. Matter*, 1995, **51**, 7299–7302.
- 13 A. Splendiani, L. Sun, Y. Zhang, T. Li, J. Kim, C.-Y. Chim, G. Galli and F. Wang, *Nano Lett.*, 2010, **10**, 1271–1275.
- 14 W. H. Baugher, H. O. H. Churchill, Y. Yang and P. Jarillo-Herrero, *Nano Lett.*, 2013, **13**, 4212–4216.
- 15 J. Zhang, H. Yu, W. Chen, X. Tian, D. Liu, M. Cheng, G. Xie, W. Yang, R. Yang, X. Bai, D. Shi and G. Zhang, *ACS Nano*, 2014, **8**, 6024–6030.
- 16 J. Jeon, S. K. Jang, S. M. Jeon, G. Yoo, Y. H. Jang, J.-H. Park and S. Lee, *Nanoscale*, 2015, **7**, 1688–1695.
- 17 Y. Yu, C. Li, Y. Liu, L. Su, Y. Zhang and L. Cao, *Sci. Rep.*, 2013, **3**, 1866.
- 18 X. Wang, H. Feng, Y. Wu and L. Jiao, *J. Am. Chem. Soc.*, 2013, **135**, 5304–5307.
- 19 T. F. Jaramillo, K. P. Jørgensen, J. Bonde, J. H. Nielsen, S. Horch and I. Chorkendorff, *Science*, 2007, **317**, 100–102.
- 20 D. Gopalakrishnan, D. Damien and M. M. Shaijumon, *ACS Nano*, 2014, **8**, 5297–5303.
- 21 J. Shi, D. Ma, G.-F. Han, Y. Zhang, Q. Ji, T. Gao, J. Sun, X. Song, C. Li, Y. Zhang, X.-Y. Lang, Y. Zhang and Z. Liu, *ACS Nano*, 2014, **8**, 10196–10204.
- 22 D. Gopalakrishnan, D. Damien, B. Li, H. Gullappalli, V. K. Pillai, P. M. Ajayan and M. M. Shaijumon, *Chem. Commun.*, 2015, **51**, 6293–6296.
- 23 A. Bruix, H. G. Füchtbauer, A. K. Tuxen, A. S. Walton, M. Andersen, S. Porsgaard, F. Besenbacher, B. Hammer and J. V. Lauritsen, *ACS Nano*, 2015, **9**, 9322–9330.
- 24 H. Schweiger, P. Raybaud, G. Kresse and H. Toulhoat, *J. Catal.*, 2002, **207**, 76–87.
- 25 M. V. Bollinger, K. W. Jacobsen and J. K. Nørskov, *Phys. Rev. B: Condens. Matter*, 2003, **67**, 085410.
- 26 J. V. Lauritsen, M. V. Bollinger, E. Lægsgaard, K. W. Jacobsen, J. K. Nørskov, B. S. Clausen, H. Topsøe and F. Besenbacher, *J. Catal.*, 2004, **221**, 510–522.
- 27 S. Pavlović and F. M. Peeters, *Phys. Rev. B: Condens. Matter*, 2015, **91**, 155410.
- 28 J. V. Lauritsen, J. Kibsgaard, S. Helveg, H. Topsøe, B. S. Clausen, E. Lægsgaard and F. Besenbacher, *Nat. Nanotechnol.*, 2007, **2**, 53–58.
- 29 T. Weber, J. C. Muijsers, J. H. M. C. van Wolput, C. P. J. Verhagen and J. W. Niemantsverdriet, *J. Phys. Chem.*, 1996, **100**, 14144–14150.
- 30 M. A. Albitar, R. Huirache-Acuña, F. Paraguay-Delgado, J. L. Rico and G. Alonso-Nuñez, *Nanotechnology*, 2006, **17**, 3473.
- 31 S. Bertolazzi, D. Krasnozhan and A. Kis, *ACS Nano*, 2013, **7**, 3246–3252.
- 32 S. Tiwari, F. Rana, K. Chan, L. Shi and H. Hanafi, *Appl. Phys. Lett.*, 1996, **69**, 1232–1234.
- 33 H. I. Hanafi, S. Tiwari and I. Khan, *IEEE Trans. Electron Devices*, 1996, **43**, 1553–1558.
- 34 N.-M. Park, S.-H. Jeon, H.-D. Yang, H. Hwang, S.-J. Park and S.-H. Choi, *Appl. Phys. Lett.*, 2003, **83**, 1014–1016.
- 35 T.-C. Chang, F.-Y. Jian, S.-C. Chen and Y.-T. Tsai, *Mater. Today*, 2011, **14**, 608–615.
- 36 R. Yang, C. Zhu, J. Meng, Z. Huo, M. Cheng, D. Liu, W. Yang, D. Shi, M. Liu and G. Zhang, *Sci. Rep.*, 2013, **3**, 2126.
- 37 L. Bagolini, A. Mattoni, G. Fugallo, L. Colombo, E. Poliani, S. Sanguinetti and E. Grilli, *Phys. Rev. Lett.*, 2010, **104**, 176803.
- 38 Y. Yu, Y. Yu, Y. Cai, W. Li, A. Gurarslan, H. Peelaers, D. E. Aspnes, C. G. Van de Walle, N. V. Nguyen, Y.-W. Zhang and L. Cao, *Sci. Rep.*, 2015, **5**, 16996.
- 39 E. Lusky, Y. Shacham-Diamand, A. Shappir, I. Bloom, G. Cohen and B. Eitan, in Proceedings of 42nd IEEE Annual International Reliability Physics Symposium, Phoenix, April, 2004, pp. 527–530.
- 40 Y. C. Song, X. Y. Liu, Z. Y. Wang, K. Zhao, G. Du, J. F. Kang, R. Q. Han, Z. L. Xia, D. Kim and K. H. Lee, in Proceedings of 13th International Conference on Simulation of Semiconductor Processes and Devices, Hakone, September, 2008, pp. 41–44.
- 41 M. Sup Choi, G.-H. Lee, Y.-J. Yu, D.-Y. Lee, S. Hwan Lee, P. Kim, J. Hone and W. Jong Yoo, *Nat. Commun.*, 2013, **4**, 1624.
- 42 M. Kang, Y.-A. Kim, J.-M. Yun, D. Khim, J. Kim, Y.-Y. Noh, K.-J. Baeg and D.-Y. Kim, *Nanoscale*, 2014, **6**, 12315–12323.
- 43 J. Wang, X. Zou, X. Xiao, L. Xu, C. Wang, C. Jiang, J. C. Ho, T. Wang, J. Li and L. Liao, *Small*, 2015, **11**, 208–213.
- 44 J. P. Perdew, K. Burke and M. Ernzerhof, *Phys. Rev. Lett.*, 1996, **77**, 3865–3868.
- 45 J. P. Perdew, K. Burke and M. Ernzerhof, *Phys. Rev. Lett.*, 1997, **78**, 1396–1396.
- 46 S. Grimme, J. Antony, S. Ehrlich and H. Krieg, *J. Chem. Phys.*, 2010, **132**, 154104.
- 47 G. Kresse and J. Furthmüller, *Phys. Rev. B: Condens. Matter*, 1996, **54**, 11169–11186.
- 48 H. J. Monkhorst and J. D. Pack, *Phys. Rev. B: Solid State*, 1976, **13**, 5188–5192.